Structure Sensitivity and Evolution of Nickel-Bearing Nitrogen-Doped Carbons in the Electrochemical Reduction of CO$_2$

Simon Büchele,[†]   *Antonio J. Martín,*[†]   *Sharon Mitchell,*[†]   *Frank Krumeich,*[‡]   *Sean M. Collins,*[§]
Shibo Xi,[#] *Armando Borgna,*[#] *Javier Pérez-Ramírez*[*,†]

[†] Institute for Chemical and Bioengineering, Department of Chemistry and Applied Biosciences, ETH Zürich, Vladimir-Prelog-Weg 1, 8093 Zürich, Switzerland.

[‡] Laboratory of Inorganic Chemistry, Department of Chemistry and Applied Biosciences, ETH Zürich, Vladimir-Prelog-Weg 1, 8093 Zürich, Switzerland.

[§] Department of Materials Science and Metallurgy, University of Cambridge, CB3 0FS Cambridge, United Kingdom.

[#] Institute of Chemical and Engineering Sciences, Agency for Science, Technology and Research (A*STAR), 1 Pesek Road, Jurong Island, 627833 Singapore.

ABSTRACT

The emergence of nickel single-atoms on nitrogen-doped carbons as high-performance catalysts amenable to rationalization due to their well-defined structure could lead to applicable technologies for the electrocatalytic CO_2 reduction reaction (eCO$_2$RR). However, real materials are unlikely to display a uniform site structure, which limits the scope of current efforts focused on idealized models for future implementation. Here, we prepare distinct nickel entities (single atoms or nanoparticles) on nitrogen-doped carbons and evaluate them in eCO$_2$RR. Single atoms demonstrate a characteristic high selectivity to CO. However, this is not altered by the presence of metal nanoparticles formed upon reducing the nitrogen content of the carrier. In contrast, nanoparticles incorporated via a colloidal route promote the parasitic hydrogen evolution reaction. In these systems, the CO selectivity evolves upon repeated exposure to potential, reaching values comparable to single atoms. By introducing CO stripping voltammetry as a characterization tool for this class of materials, we identify a decreased metallic surface, suggesting that the nanoparticle surface is altered by CO. The findings highlight the critical role of dynamic effects in catalyst design for eCO$_2$RR.

1. INTRODUCTION

The electrocatalytic CO_2 reduction reaction (eCO₂RR) is widely explored, due to its potential to contribute to valorizing this greenhouse gas, closing the anthropogenic carbon cycle. Depending on the catalytic system and operation conditions, a variety of products (e.g. CO, $HCOO^-$, alcohols, and hydrocarbons) can be obtained.[1-2] Performing this reaction in aqueous electrolytes is desirable but challenging since commonly studied transition metals often exhibit appreciable activity in the parasitic hydrogen evolution reaction (HER).[3] In bulk form, these systems typically require considerable overpotentials to reach practical current densities that are of practical relevance for the eCO₂RR because of suboptimal adsorption energies of intermediates arising from linear scaling relations between them.[4-6] Different approaches to circumvent these scaling laws include (near) surface alloying,[7-8] functionalization with surface-anchored ligands,[9] modification with chalcogens,[10] or downsizing of supported metal particles into single-atom catalysts (SACs).[11-13] Despite significant experimental and theoretical progress toward establishing catalyst design guidelines, the development of scalable, high performing materials still mostly relies on serendipitous catalyst discovery.

In this context, various transition metals including Mn, Fe, Co, Ni, and Co, atomically dispersed on conductive hosts have been applied targeting eCO₂RR.[14-17] Nickel and iron SACs based on nitrogen-doped carbons have attracted particular interest in recent years, promoting the almost exclusive production of carbon monoxide. These systems provide a prototypical platform for studying structure-activity relations since they tend to favor simpler two-electron reduction mechanisms.[18] Besides, the electronic state and coordination environment of the metal atoms in these sites can be modified to a considerable degree through the synthesis route.[19-22] Seminal works for nickel date back to 2016, showing drastically different selectivity patterns for Ni-SACs

when compared to bulk metal.[23] Since then, a vast amount of research has gathered a more precise mechanistic understanding through in situ characterization and calculations.[14,24-28] In parallel, the selectivity of these materials could be optimized, reaching almost full Faradaic efficiencies for CO at mild overpotentials (FE_{CO} = 97 % at −0.5 V vs. RHE),[25] whereas current densities are approaching industrially profitable levels (> 300 mA cm^{-2} retaining high FE_{CO}), albeit with insufficient energy efficiency (<50%). [29-30] While the gram-scale synthesis of Ni-SACs has been reported,[31] it is still unclear how translatable this will be for industrial manufacture.

However, nickel-based materials are also considerably active toward the parasitic HER.[32] Therefore, metallic nanoparticles are regarded as detrimental, posing a challenge for the development of practical and selective SACs for the eCO$_2$RR, since their industrial manufacture may demand extensive efforts in synthesis and characterization to ensure the exclusive presence of stable isolated metal species.[33-35] Alternatively, a few studies have claimed nickel nanoparticles intentionally coated with a thick (nitrogen-doped) carbon layer can exhibit eCO$_2$RR activity, although the presence of atomically dispersed nickel could not be excluded from the data presented.[36-37]

To gain insight into the structure sensitivity of nickel-bearing catalysts in this reaction, we target distinct metal speciation by deposition of colloidal nanoparticles or impregnation by nickel acetate on carbons and their nitrogen-doped analogues. Evaluation in eCO$_2$RR demonstrates that particles originating from impregnation do not negatively affect FE_{CO}, whereas colloidal particles promote the HER, questioning the dogma that nickel particles are detrimental for selectivity. Furthermore, colloidal particle-based catalysts evolve upon repeated chronoamperometries, leading to an increase in selectivity reaching similar values to nickel SACs. Due to the evolution

in the performance observed, specific emphasis is placed on understanding the impact and nature of dynamic effects which are rarely addressed in electrocatalysis.[38-40] To this end, we introduce CO stripping voltammetry to identify a descriptor for highly performing materials.

2. EXPERIMENTAL

2.1. Synthesis of Nickel Colloid. A suspension of uniformly sized nickel nanoparticles was synthesized adapting a literature method.[41] Nickel acetylacetonate (0.51 g, Acros Organics, 96%) was mixed with oleylamine (30 cm^3, Sigma Aldrich, 70%) and oleic acid (0.64 cm^3, Sigma Aldrich, 90%) and degassed under an Ar flow for 40 min. The mixture was heated to 383 K and kept at this temperature for 60 min. After cooling to 363 K, borane triethylamine complex (0.24 g, Sigma Aldrich, 96%) dissolved in oleylamine (4 cm^3) was quickly added to the mixture. The mixture turned black after 60 min. Analysis by TEM (**Figure S1**) confirmed a narrow particle size distribution with an average diameter of 3.6 nm.

2.2. Catalyst Synthesis. Carbon-based hosts and nitrogen-doped analogues were synthesized following a previously reported recipe.[19] Briefly, carbon nanofibers (graphitized, iron free, D × L 100 nm × 20-200 μm, Sigma-Aldrich) were treated in a mixture of concentrated H_2SO_4:HNO_3 (66:33 cm^3 g_{carbon}^{-1}) at 343 K for 2 h, washed with water (1 dm^3 g_{carbon}^{-1}), and dried at 338 K. To prepare nitrogen-doped carbons, the resulting material (1 g) was mixed with dicyandiamide (3 g, 99 %) and water (40 cm^3), followed by sonication for 0.5 h at 323 K. The resulting dispersion was freeze dried then heated (Carbolite tubular oven) to 723 K (5 K min^{-1}) for 2 h under N_2 flow and successively to either 923 or 1223 K (5 K min^{-1}) for 3 h, obtaining NC_{923} and NC_{1223}. The undoped carbon (C_{1223}) was obtained by the same procedure but without the addition of dicyandiamide.

Ni$_{IMP}$-based samples were prepared by mixing nickel acetate tetrahydrate (10.6 mg, 99.7 %) with water (50 cm^3) before adding the carbon host (500 mg) under stirring. In the case of Ni$_{CNP}$-based samples, the host (500 mg) was dispersed in ethanol (31.25 g) by sonication for 10 min before slowly adding the nickel colloid (31.25 g) under stirring. The obtained dispersions were subsequently heated at 338 K until the solvent completely evaporated. The resulting powders were heated to 573 K (5 K min^{-1}) for 5 h in an IR tubular oven (behr Labor-Technik) under N$_2$ flow to obtain the catalyst. For the acid leaching, the as synthesized catalyst (100 mg) was mixed with 1 M H$_2$SO$_4$ (100 cm^3), sonicated for 30 min, and heated to 343 K overnight. After cooling, the catalyst was filtered, washed with 1 M H$_2$SO$_4$ (100 cm^3) and ultrapure water (500 cm^3), and dried at 338 K.

2.3. Electrode Preparation. The electrodes were prepared by airbrushing a catalyst ink on a gas diffusion layer (GDL) carbon paper. The ink was prepared by ultrasonic dispersion of the catalyst (50 mg) in a mixture of water (4 cm^3), isopropanol (4 cm^3) and 5 wt.% Nafion solution (0.05 cm^3) for 45 min. The ink was then deposited on the microporous layer of a GDL carbon paper (35BC, S110GL group, 12 cm^2 cross-sectional area) mounted on a hotplate at 353 K using an airbrush (Iwata Eclipse HP - SBS). A catalyst loading of 0.8-1.2 mg cm^{-2} was typically achieved. The final electrodes were produced by cutting the GDL electrode in L-shaped pieces of ca. 2 cm^2 and attaching them to a glassy carbon piece using Kapton tape to secure the electrical connection. The electrodes were photographed, and their total geometric area determined with the Image J software (Wayne Rasband, National Institutes of Health).

2.4 Spectroscopy and Diffraction Analysis. XRD was conducted using a PANalytical X'Pert PRO-MPD diffractometer operated in Bragg-Brentano geometry applying Ni-filtered Cu Kα radiation ($\lambda = 0.1541$ nm). Data was collected in the range 5 - 70° 2θ (0.05° and 1.5 s per step).

Raman spectroscopy was performed with a confocal Raman microscope (WITec CRM 200) operated in backscattering mode at a power of 6 mW using a wavelength of 532 nm and a 100× objective lens. XPS was performed on a Thermo Scientific Sigma 2 spectrometer equipped with a hemispherical electron-energy analyzer operated at constant pass energy (25 eV) using polychromatic Al Kα radiation (50° emission angle; 2×10^{-8} mbar residual pressure) in large area mode. Prior to the measurement, catalyst powders were pressed onto round custom-made aluminum sample holders (diameter 10 mm). A Shirley type background was subtracted before data comparison. The analysis of the nickel 2 p XPS signal on electrodes was not possible due to the spectral interference with the Auger signal of either fluorine (from Nafion) or nitrogen (from NC). Ni LMM Auger spectra (AES) were collected using equivalent settings. The position of the Auger peak was determined as the point of highest intensity after background subtraction. The Ni K-edge X-ray absorption spectra were measured at the XAFCA beamline of the Singapore Synchrotron Light Source (SSLS).[42] The storage ring of the SSLS was operated at 0.7 GeV with a maximum current of 200 mA. The measurements were performed in transmission mode for fresh catalysts using a Si(111) double-crystal monochromator and in fluorescence mode for used electrodes with a silicon drift detector (Bruker XFlash Detector 6|100). Energy calibration was done using Ni foil-K-edge spectrum as the reference. The X-ray absorption data were processed and analyzed and fitted (parameters in **Table S1**) using Demeter software.[43] The K- and R-ranges for the fitting were set as 2-10.5 Å^{-1} and 1-3 Å, respectively. ICP-OES was measured on a Horiba Ultra 2. Catalyst powders were digested in an MLS turboWave microwave by heating the material (ca. 10 mg) in HNO_3 (65 wt.%, 3 cm^3) and H_2O_2 (35 wt.%, 1 cm^3) to 533 K for 25 min with a maximum power of 1200 W and a loading pressure of 70 bar. The obtained clear solutions were filtered (Chromafil Xtra PTFE-45/25, 0.45 μm) and diluted to 25 cm^3 prior to

analysis. Static volumetric chemisorption with CO (Messer 99.997%) was performed at 308 K using a Micromeritics 3Flex Chemi instrument. The chemisorbed amount was calculated from the difference of two consecutive CO sorption isotherms (1st chemisorption and physisorption; 2nd only physisorption) with intermediate evacuation for 1 h. Prior to the chemisorption the materials were heated in vacuum at 383 K for 30 min, consecutively reduced in hydrogen flow (50 cm^3 min^{-1}, PanGas, purity 5.0) at 673 K for 30 min and evacuated at 673 K for 30 min.

2.5. Electron Microscopy. HAADF-STEM investigations were performed on a Talos F200X instrument (200 kV, colloidal nickel) or a Hitachi HD-2700CS (200 kV, cold field emitter) in high-angle annular dark field mode (**Figure 1** and **Figure 5b**). An energy-dispersive X-ray spectrometer (EDAX) attached to the microscope column was used for analytical investigations. High-resolution ADF-STEM imaging of fresh and used samples was carried out using a JEOL ARM300CF microscope (60 kV, convergence semi-angle approximately 30.6 mrad) equipped with a cold field emission source and aberration correctors in both the probe-forming and image-forming optics, located in the electron Physical Sciences Imaging Centre (ePSIC) at the Diamond Light Source. The direct beam disk was centered on the ADF detector with a camera length selected such that the inner collection angle was just beyond the direct beam disk. A 3 mm BF aperture was inserted to limit the collection angle of the BF-STEM detector to approximately the inner half of the direct beam disk. The optical settings were selected to balance contrast from the low atomic number carbon fibers and the higher atomic number Ni species while maximizing the signal collected per incident electron to reduce the dose required for high quality imaging and to minimize electron beam induced damage. In all cases, samples were prepared on lacey carbon grids by first sonicating powders (or powders scraped from electrode surfaces) in isopropyl

alcohol or ethanol for 1 min followed by drop casting. The nickel colloid was directly drop casted onto the grid.

2.6. Electrocatalytic Measurements. A custom gastight glass cell with two compartments separated by a Selemion AMV anion exchange membrane (AGC engineering) or a Nafion 212 membrane (Alfa Aesar) was employed for all electrochemical experiments (**Figure S2**). Each compartment contained electrolyte (40 cm^3, 0.1 M KHCO$_3$) and was saturated with CO$_2$ (Messer, purity 4.8) for at least 30 min prior to the start of the eCO$_2$RR experiments, with a resulting pH of 6.7. CO$_2$ was continuously bubbled into the catholyte during the electrolysis at a flowrate of 20 cm^3 min^{-1}. Measurement without the addition of CO$_2$ were carried out in 0.1 M phosphate buffer (Na$_2$HPO$_4$/NaH$_2$PO$_4$, pH = 6.8) to maintain comparable conditions. All electrochemical measurements were carried out at room temperature with an Autolab PGSTAT302N potentiostat, using a platinum wire as the counter electrode and an Ag/AgCl reference electrode (saturated KCl, model RE-1CB, ALS). All potentials reported in this work are referenced to the reversible hydrogen electrode (RHE) scale. Double-layer (DL) capacitances of the electrodes were estimated by performing cyclic voltammetries (CVs) at different scan rates (typically 2, 4, 6, 8, 10, and 15 mV s^{-1}) narrowly centered (30 mV) at the open-circuit potential (OCP) before and after electrolysis, following full stabilization of the CV response. Potentiostatic electrolyses were carried out at −0.6 V vs. RHE with the ohmic voltage drop compensation function set at 85% of the uncompensated resistance (R_u), which was determined before the start of the electrolysis and updated every 10 min by electrochemical impedance spectroscopy (EIS) measurements during the electrolysis. The recorded potentials were converted to the RHE scale following the electrolysis after manually correcting for the remaining uncorrected R_u. Following this correction, the applied potentials were within 10 mV of the target potential of the electrolysis.

The reported activities were normalized to the values of double layer capacitance measured after reaction (**Table S2**) to account for differences in surface wetting.[44] For the analysis of the gas phase reaction products, the outlet gas of the cathodic compartment of the cell flowed continuously through the sample loop of an SRI 8610C gas chromatograph (Multi-Gas #3 configuration) operating with Ar as carrier gas at a head pressure of 2.3 bar and equipped with HayeSep D and Molecular Sieve 13X packed columns. In all eCO$_2$RR tests hydrogen and carbon monoxide were the only observed product. The respective Faradaic efficiencies were calculated by relating the amount produced to the total charge passed during the electrolysis. Partial current densities for each product i (i = CO or H$_2$) were obtained as described in Equation (1).

$$j_i = V_{gas} \text{ (mol s}^{-1}\text{)} \times c_i \text{ (mol mol}^{-1}\text{)} \times 2 \text{ F} \tag{1}$$

where V_{gas} is the flow of CO$_2$ or Ar bubbled through the cell, c_i is the concentration obtained from GC analysis, 2F is the charge required to produce 1 mol of product, with F being the Faraday constant. Error bars for currents and Faradaic efficiencies represent the standard deviation obtained from multiple independent measurements. To test the catalyst evolution during consecutively repeated reactions, the following procedure was applied: First potentiostatic electrolysis at −0.6 V vs. RHE was carried out with product quantification after 30 min. The system was then left to relax to OCP for at least 15 min before determining the DL capacitance and conducting CVs for 10 cycles at a scan rate of 20 mVs^{-1}.

2.7. CO Stripping Voltammetry. For this analysis the same setup was used as for the electrocatalytic measurements filled with 0.1 M phosphate buffer. The cell was first saturated with CO (Messer, 99.997%) by bubbling the gas into the catholyte at 20 cm^3 min^{-1} for 30 min while stirring. Then the system was kept at −0.6 V vs. RHE under potentiostatic control while bubbling CO at 20 cm^3 min^{-1} for 20 min to allow the adsorption of the gas onto the reduced

metal surface followed by bubbling Ar (Messer, purity 5.0) at $20 \, cm^3 \, min^{-1}$ for 20 min to remove solvated and weakly bound CO. Without turning off the potentiostat in between, three consecutive potential sweeps between -0.6 and 1.7 V vs. RHE were then conducted, monitoring the oxidation current of adsorbed CO species. For data analysis, the difference between the first and second anodic sweeps was calculated, and a background fitted by spline interpolation was subtracted.

3. RESULTS AND DISCUSSION

3.1. Synthetic Approach and General Characterization. To assess the structure sensitivity, a series of nickel catalysts was synthesized, targeting the dominant presence of either nanoparticles (Ni_{CNP}-based samples) or atomically dispersed nickel (Ni_{IMP}-based samples) on C or NC through distinct approaches (**Scheme 1**). Additionally, the nitrogen content of NC was varied by changing the doping temperature to tune the degree of stabilization for atomically dispersed nickel. Further samples were derived by leaching with sulfuric acid (denoted as "-L"),[14] leading to virtually particle-free materials. Successful nitrogen-doping is confirmed by analysis of the XPS signals shown in **Table 1** and **Figure S3** , where the contributions from different nitrogen species are quantified.[19,45] Pyridinic and pyrrolic species are dominant in NCs prepared at low temperature, while quaternary nitrogen species account for an increased relative concentration at high temperature due to their higher thermal stability.[46] The surface nitrogen content varies from 1.2 wt.% ($T = 1223$ K) to 10.7 wt.% ($T = 923$ K), the lower doping temperature providing more potential anchoring sites for atomically dispersed nickel. We remark
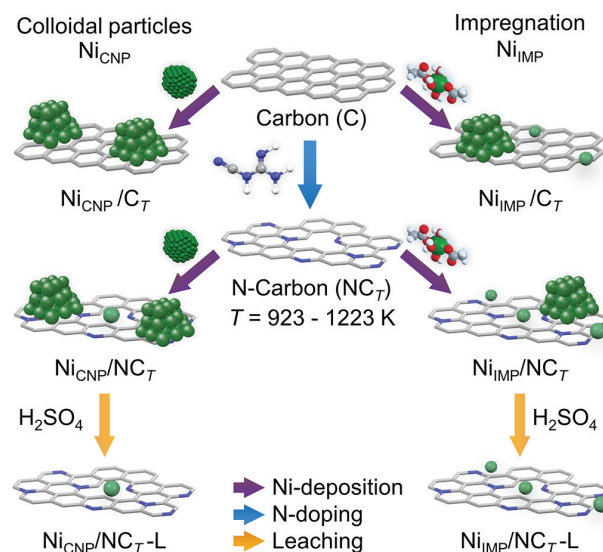
Scheme 1. Synthetic routes to examine the structure sensitivity of nickel supported on carbon nanofibers (C) and nitrogen-doped analogues (NC), obtained by post-synthetic heat treatment with dicyandiamide. The corresponding sample nomenclature is indicated. Color code: grey, C; blue, N; green, Ni.

that acid leaching does not significantly affect the nitrogen speciation. Regarding crystallinity, Raman spectroscopy suggests that all samples are relatively ordered displaying a small I_D/I_G ratio, and contain an appreciable amount of graphitic carbon, as deduced from XRD (**Figure S4**). No reflections for metallic nickel were observed, compatible with the relatively low loading and small particle size. The scalable synthetic approach applied here provides a flexible platform for tuning catalyst characteristics to develop structure-activity relations.

3.2. Nickel Speciation. To assess the presence of distinct nickel entities we first performed extensive analysis by aberration corrected scanning transmission electron microscopy in high-angle annular dark field mode (HAADF-STEM). As expected, particles could be clearly observed on samples obtained via the colloidal route (Ni_{CNP}/C_{1223}, Ni_{CNP}/NC_{923}, Ni_{CNP}/NC_{1223}) and the impregnated NC with low nitrogen content (Ni_{IMP}/NC_{1223}). They all displayed a similar

average diameter of ca. 5 nm throughout (**Table 1** and **Figure 1**). For Ni_{CNP}-based catalysts this is slightly larger than the size of the colloidal precursor, pointing out that some particles might have sintered during the deposition process. In contrast, no particles could be detected on Ni_{IMP}/NC_{923}, in line with the increased concentration of anchoring surface nitrogen species. Particles are also not observed on the nitrogen-free Ni_{IMP}/C_{1223}, but metallic behavior is clearly detected by CO stripping voltammetry (see below). The absence of virtually all particles in acid leached samples (Ni_{CNP}/C_{1223}-L and Ni_{IMP}/C_{1223}-L) confirms the efficiency of the procedure. However, the overall metal content is also drastically reduced, suggesting that a sizable proportion of the potentially active nickel single atoms might also have been leached and hence underscoring an undesired effect of this commonly applied synthetic step.

Table 1. Elemental surface composition and nickel particle size in the catalysts.

Sample	Ni_{total} (wt.%)[a]	$Ni_{surface}$ (wt.%)[b]	$C_{surface}$ (wt.%)[b]	$N_{surface}$ (wt.%)[b]	$O_{surface}$ (wt.%)[b]	d (nm)[c]
Ni_{CNP}/C_{1223}	1.51	4.2	91.4	0.0	4.4	5.0
Ni_{CNP}/NC_{923}	1.73	8.7	77.2	8.8	5.3	5.0
Ni_{CNP}/NC_{1223}	1.26	2.5	93.4	1.1	3.0	4.8
Ni_{CNP}/NC_{1223}-L	0.05	0.1	95.4	1.9	2.6	-
Ni_{IMP}/C_{1223}	0.39	0.8	98.0	0.0	1.2	-
Ni_{IMP}/NC_{923}	0.48	3.3	82.6	10.7	3.3	-
Ni_{IMP}/NC_{1223}	0.39	1.9	94.3	1.3	2.5	4.8
Ni_{IMP}/NC_{1223}-L	0.01	0.0	97.0	1.2	1.8	-

[a]Determined by ICP-OES. [b]Determined by XPS. [c]Average particle size determined by STEM.
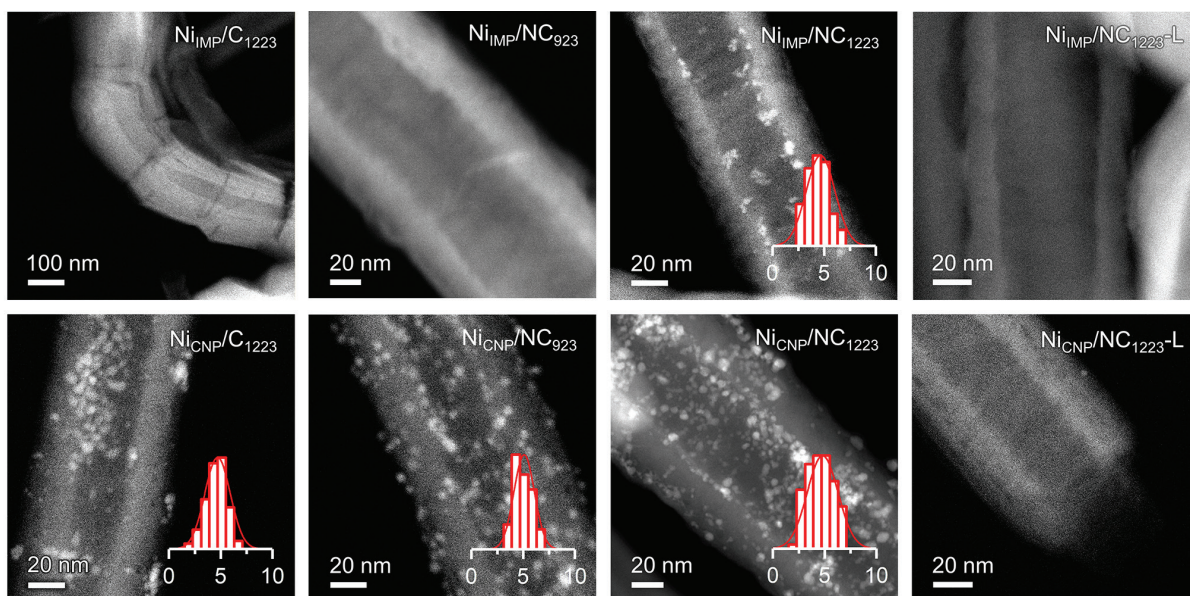
Figure 1. HAADF-STEM images of Ni_{CNP}-based (bottom) and Ni_{IMP}-based (top) catalysts. Particle size distributions (in nm) are shown inset where relevant.

Concerning the presence of atomically dispersed nickel, aberration corrected STEM analyses at high spatial resolution (**Figure 2** and **Figures S5-S8**) evidences the presence of isolated metal centers in both Ni_{IMP}- and Ni_{CNP}-based samples, albeit to different degrees, and thus explaining the activity toward CO production (see below).[18] In more detail, single atoms can be identified on all particle-containing NCs (**Figure 2** and **Figures S5-S6**) whereas only atomically dispersed species are visible in Ni_{IMP}/NC_{923} (**Figure S7**). Some nickel single atoms are discernible even in the particle rich Ni_{CNP}/C_{1223} (**Figure S8**), presumably anchored to oxygen atoms present in the carbon matrix.
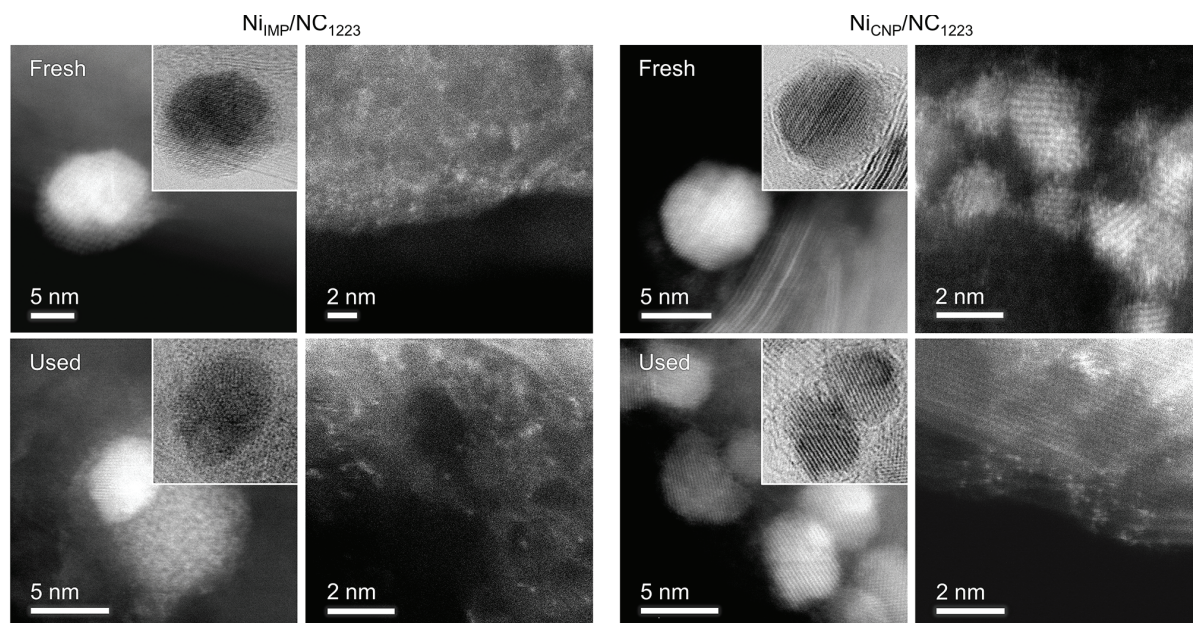
Figure 2. High resolution ADF-STEM images of fresh (top) and used (bottom, after 90 min of chronoamperometry at −0.6 V vs. RHE) catalysts assessing the presence of atomically dispersed nickel species. Corresponding BF-STEM images are displayed as insets.

To further understand the chemical state and coordination of nickel in the catalysts (**Figure 3 and S9-S10**) we analyzed the Ni $2p_{3/2}$ XPS, Ni LMM Auger, and Ni K-edge X-ray absorption spectra. All catalysts show a Ni $2p_{3/2}$ XPS peak between 855 and 856 eV, close to the expected values for nickel oxide,[47] readily ascribable to nanoparticles oxidized upon exposure to atmospheric conditions.[48] However, the claimed Ni $2p_{3/2}$ signal for single nickel atoms is also expected to be close to 855 eV,[25,29] making it challenging to distinguish distinct metal entities. Only samples containing abundant particles (Ni$_{CNP}$/NC$_{1223}$ and Ni$_{CNP}$/C$_{1223}$) show a clear signal of the oxide, reflected by a shoulder at lower binding energy. A more complete picture emerged from analysis of the Ni LMM Auger signal (**Figure S9b**) constructing a chemical state plot (i.e. BE_{XPS} vs. KE_{Auger}, also referred to as Wagner plot). In this representation, samples lying on the same diagonal line accounting for equal modified Auger parameter (defined as

$\alpha' = BE_{2p3/2} + KE_{LMM}$) are assigned to the same chemical state. When comparing with reported data it is apparent that catalysts based on C indeed show characteristics of nickel oxide,[49] whereas all catalysts on NC show a lower value of α' (**Figure S10**). In its most general sense, this parameter can be understood as a measure of covalent or ionic character, with lower values describing more ionic chemical states.[49] The observed change for NC is tentatively assigned to the more cationic character of atomically dispersed nickel species compared to the oxide. X-ray absorption near edge structure (XANES) analysis also suggest oxidized nickel species (Ni^{2+}) for almost all materials, with only Ni_{IMP}/NC_{1223}-L and Ni_{CNP}/C_{1223} showing an edge position at slightly lower energy as well as a significant pre-edge structure which is indicative of metallic nickel (Ni^0).
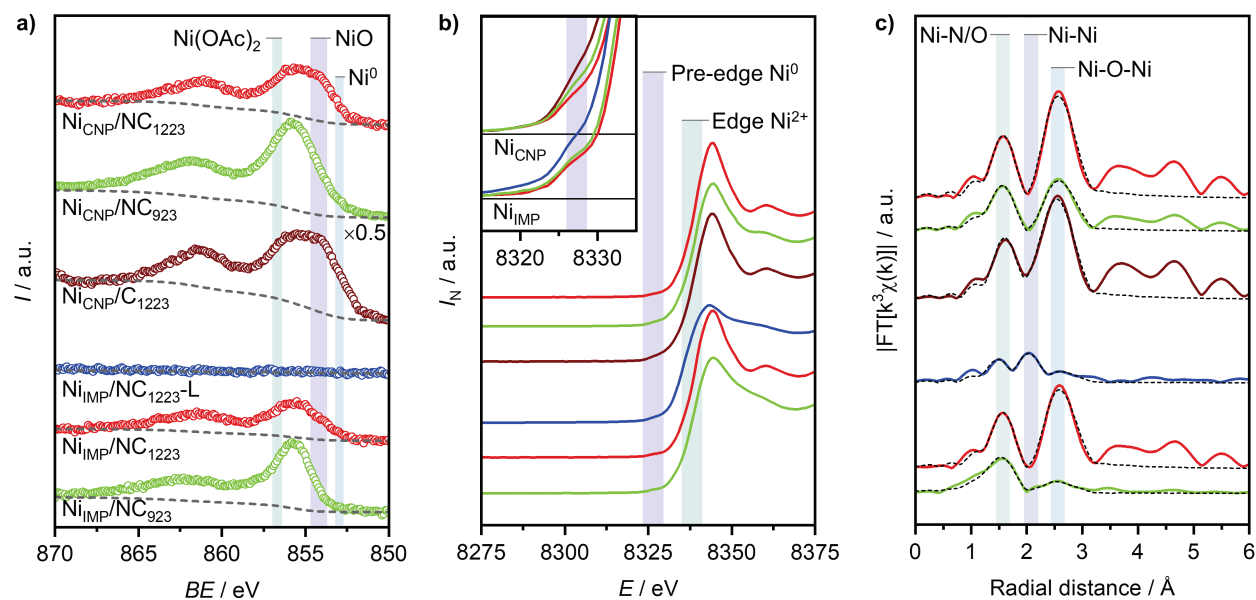

Figure 3. a) Ni $2p_{3/2}$ XPS spectra (dashed lines correspond to a Shirley background), b) normalized XANES, and c) k^3-weighted Fourier transform of the EXAFS spectra and fitted spectra (dashed lines) of selected Ni_{IMP}-based (bottom) and Ni_{CNP}-based (top) catalysts; . Sample color codes in a) also apply to b) and c).

To investigate the local coordination sphere of nickel we turned to extended X-Ray absorption fine structure (EXAFS) analysis. Three peak positions are assigned according to reference measurements (**Figure S11**), namely Ni-N or Ni-O at 1.55 Å, Ni-Ni at 2.13 Å, and Ni-O-Ni at 2.58 Å. While most samples display a spectrum very similar to nickel oxide, Ni_{IMP}/NC_{923} shows a single strong peak for Ni-N, confirming the predominate presence of atomically dispersed metal. The acid leached sample Ni_{IMP}/NC_{1223}-L shows contributions from Ni-N and Ni-Ni, which might originate from atomically dispersed nickel species and metallic nickel inside the carbon structure that was not leached but could not be observed by microscopy.

In summary, the nickel catalysts can be categorized into four groups: (1) samples based on C with a chemical state similar to NiO (Ni_{CNP}/C_{1223} and Ni_{IMP}/C_{1223}), (2) a single-atom catalyst based on NC containing N-coordinated nickel (Ni_{IMP}/NC_{923}); (3) samples based on NC containing both particles and single atoms (Ni_{IMP}/NC_{1223}, Ni_{CNP}/NC_{923}, and Ni_{CNP}/NC_{1223}); and (4) acid leached samples with no apparent particles and reduced metal content (Ni_{IMP}/NC_{1223}-L and Ni_{CNP}/NC_{1223}-L).

3.3. Structure Sensitivity in eCO₂RR. To compare the performance of the catalysts, we mapped the partial current density normalized by double layer capacitance toward CO against the one toward H_2 (**Figure 4**, bar chart in **Figure S12**) obtained upon potentiostatic catalytic tests at −0.6 V vs. RHE in 0.1 M KHCO₃ saturated with CO_2 (pH 6.8). A quick inspection already reveals the key role of nickel, in view of the negligible activity of the metal-free NC. It is also apparent that samples not doped with nitrogen (group 1) only show negligible j_{CO} but can be very active towards the HER (Ni_{CNP}/C_{1223}). This observation agrees with the expected behavior of metallic nickel particles on a support that does not strongly affect the redox properties,[32] since the metallic phase is the only stable one under applied operating conditions.[50] In contrast, the

SAC (group 2, $Ni_{IMP}/NC923$) displays lower total current but high CO selectivity ($FE_N = 82$ %), in line with expectations from literature. All samples with mixed metal entities (group 3) show significant j_{CO} indicating that the incorporation of nitrogen originates Ni-N sites active in eCO_2RR (red arrows). Interestingly, Ni_{IMP}/NC_{1223} displays high selectivity ($FE_N = 79$ %) despite the evident presence of particles, in contrast to Ni_{CNP}-based samples ($FE_N < 45$ %). Leaching of Ni_{CNP}/NC_{1223} (indicated by blue arrows, group 4) demonstrates that the selectivity can be greatly improved (albeit at lower j_{CO}) by removal of the particles, while the same procedure only reduces the activity of Ni_{IMP}/NC_{1223} without altering its selectivity. This indicates that leaching procedures might have a harmful effect on the overall activity in eCO_2RR. In parallel, we mention that samples doped at 1223 K show higher eCO_2RR activity than the ones doped at 923 K, suggesting that low nitrogen content indirectly promotes the reaction. This is likely caused by a reduced coordination of Ni-N sites, which are predicted to be more active.[27,51] The catalysts were analyzed after 90 min under reaction by high-resolution STEM (**Figure 2** and **S13-14**) to confirm the effect of the reducing electrochemical environment, evidencing the persistence of both particles and single atoms. The increased prominence of single atoms could suggest some dispersion of smaller nickel clusters, but the average particle size of nickel remains relatively constant.
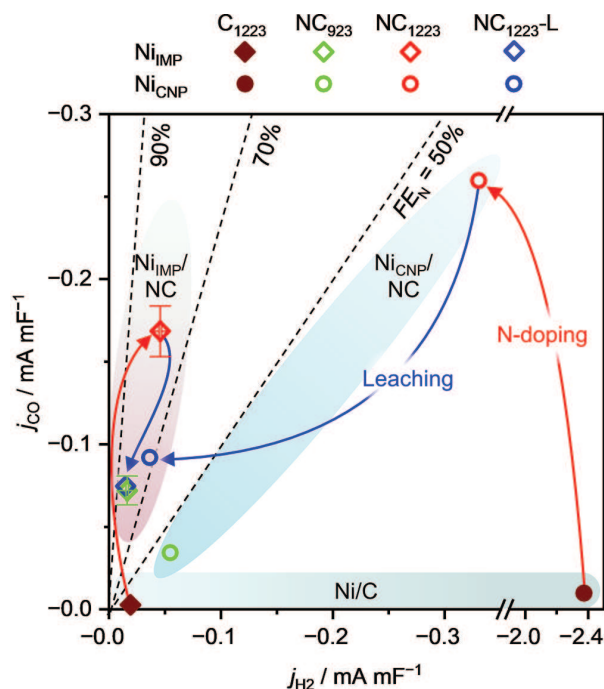
Figure 4. Performance of the nickel catalysts in the electrochemical reduction of CO_2 observed after 90 min of chronoamperometry at -0.6 V vs. RHE. Diagonal lines indicate constant normalized Faradaic efficiency towards CO, defined as $FE_N = j_{CO}/(j_{CO}+j_{H2})$. Typical performance regions of nickel on undoped (C) and nitrogen-doped (NC) carbon are shaded in color. Currents are normalized by double layer capacitance.

The unexpected result that particles formed upon impregnation do not negatively affect the selectivity openly contradicts the current belief that they should be avoided at all cost. Detailed analysis by high resolution microscopy (**Figure 1**, **S5**, and **S13**) reveals that most particles in this sample have a metallic core with a more amorphous nickel shell. This observation triggered interest in the catalysts containing distinct nickel entities and prompted further investigation of the origin of this phenomenon.

3.4. Understanding the Evolving Reactivity of Nickel Particles. Considering the critical role of catalyst stability for the development of eCO$_2$RR technologies,[1] we examined the

evolution of the performance under operating conditions. Interestingly, we discovered that systems initially catalyzing HER can evolve over time, largely losing their activity for this reaction.[40] Applying the same approach, we found that performing five consecutive reactions (i.e. cycles of 5×30 min in CO_2 saturated electrolyte at −0.6 V vs. RHE relaxing to open-circuit potential in between) provokes a progressive shift to lower j_{H2} (**Figure 5a**). This results in selectivity enhancements of up to 63%, reaching a performance close to that typically observed for impregnated materials ($FE_{N,1} = 38 \rightarrow FE_{N,5} = 62\%$ for Ni_{CNP}/NC_{1223}). Comparatively, nanoparticles in the sample synthesized by impregnation retain their spectator character but the eCO_2RR activity decreases slightly. This observed dynamic behavior could not be explained by detailed ex situ characterization of the fresh and cycled catalysts. Specifically, analysis of Ni_{CNP}/NC_{1223} by microscopy evidences only a slight reduction of the average particle size by 0.5 nm upon cycling, while no significant differences are identified by EXAFS (**Figure 5b** and **c**). Since the results implied that the variation in performance does not originate from a change in the bulk character, we directed our efforts toward assessing surface modifications on the catalytically active nanoparticles.

As mentioned, it is known that (i) metallic nickel shows very high HER activity, which explains the increased j_{H2} of Ni_{CNP}-based samples and (ii) metallic nickel strongly interacts with carbon monoxide.[52]. This made it reasonable to think that nickel nanoparticles could be poisoned by CO produced by the eCO_2RR over neighboring single atoms. Consistently, we confirmed the decreasing activity of the sample fully selective toward H_2 (Ni_{CNP}/C_{1223}) upon CO bubbling (**Figure S15**), which agrees with the reduced HER observed during the evolution of Ni_{CNP}/NC_{1223}. However, the clearly distinct catalytic evolution during the cycling procedure between the particles arising from impregnation and those directly deposited suggested a more

complex picture. Based on this reasoning, we put forward that spectator particles may interact less strongly with CO, showing a vastly different behavior than bulk metal.
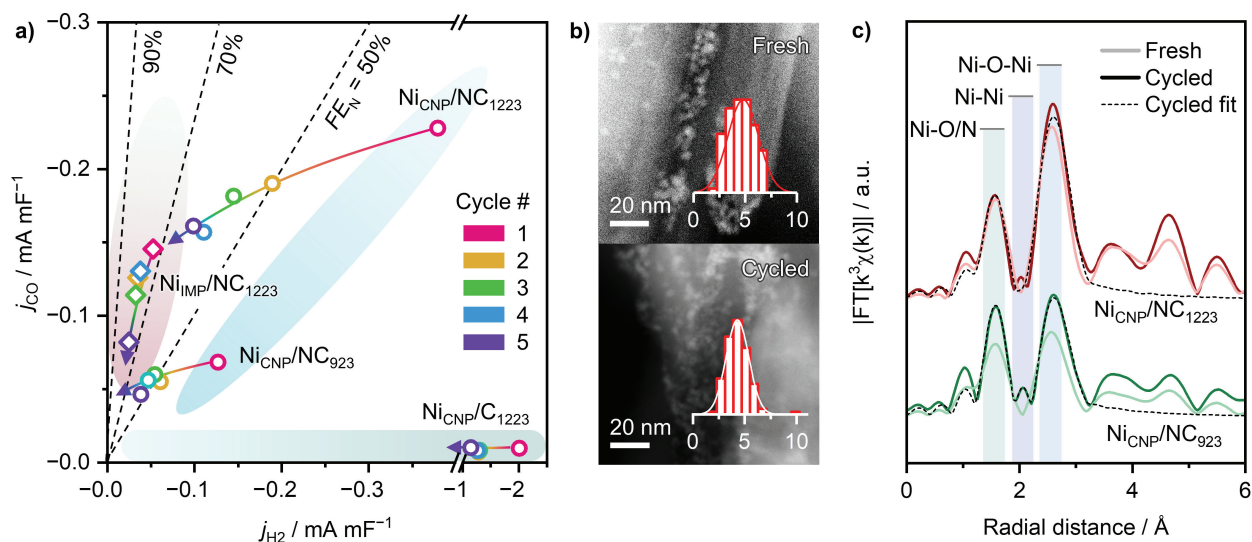

Figure 5. a) Evolution of the activity during exposure to 5 cycles of potentiostatic electrolysis (30 min, −0.6 V vs. RHE) followed by relaxation to OCP (1-5). Diagonal lines and shaded regions are defined in **Figure 4**. b) HAADF-STEM of fresh and cycled Ni_{CNP}/NC_{1223} with corresponding particle size distribution (in nm) inset. c) k^3-weighted Fourier transform of the EXAFS spectra of selected fresh and cycled nanoparticle-based catalysts.

To test this hypothesis, we adapted a widely used tool in fundamental electrochemical research on Pt surfaces, namely CO stripping voltammetry.[53] For this in situ technique, CO is first adsorbed on the metal at a favorable potential (−0.6 V vs. RHE herein) by bubbling the gas into the electrochemical cell. Subsequently the oxidation of adsorbed CO is monitored during an anodic sweep, evidenced by a peak in the voltammogram (**Figure 6**). The magnitude and position of the CO oxidation peak provide information about the reacting surface area and the strength of CO-metal interaction, respectively. Measurement of a Ni wire reveals two signals at

0.30 V and 0.56 V vs. RHE ascribed to the oxidation of nickel ($Ni^0 \rightarrow Ni^{2+}$),[54] and CO

($CO \rightarrow CO_2$), respectively (**Figure S16**). Regarding Ni_{CNP}-based materials, i.e. samples with

large j_{H2}, they all show a CO oxidation peak, confirming the presence of nickel surface with bulk

metallic character. Nevertheless, the corresponding cycled samples do not show a CO oxidation

peak, indicating a structural change upon evolution. Interestingly, CO oxidation peaks could not

be detected on selective Ni_{IMP}-based NCs before or after cycling, indicating a different

interaction of the nanoparticles with CO. In addition, the same peak, albeit at much lower

intensity, is observed for the nickel impregnated sample on C (Ni_{IMP}/C_{1223}), agreeing with the

chemical state analysis suggesting the presence of particles not detected by electron microscopy.

Finally, a peak for Ni/Ni^{2+} is apparent for Ni_{CNP}/C_{1223} which can be caused by a partial CO

coverage of the nickel surface (**Figure S15**).

The CO stripping voltammetry also enables the determination of the electrochemically

exposed metallic nickel surface area which could be a useful normalization parameter assessing

the activity of specific sites. However, this is not possible in the systems presented herein, since

the technique is insensitive to atomically dispersed species or restructured nanoparticles.

Similarly, conventional techniques like CO chemisorption fail to assess the dispersion of single

nickel atoms (**Figure S18**). This emphasizes the need for improved characterization methods

applicable to SACs, the development of which is beyond the scope of the current study.

Importantly, the main trends reported herein are not affected by the normalization of the current
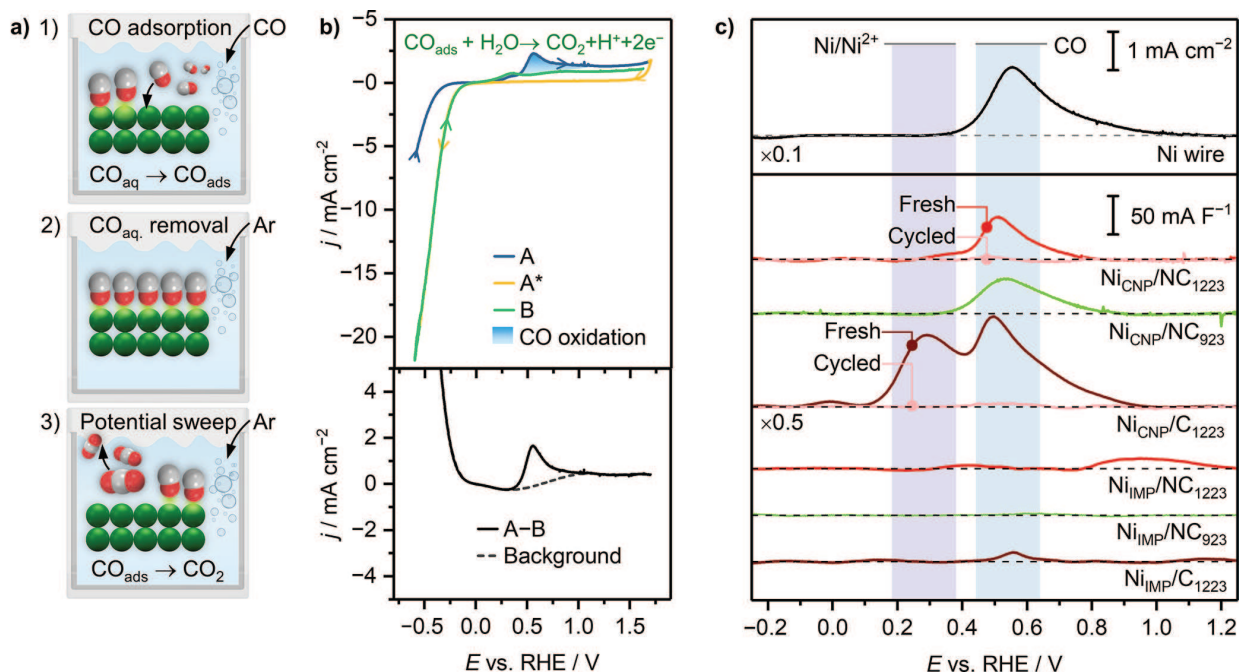
(**Figure S19-S21**).

Figure 6. a) CO stripping voltammetry. a) Schematic of the experimental procedure applied before obtaining CVs. Color codes: grey, C; red, O; green Ni; blue, electrolyte. b) Approach to data treatment starting from the acquired CVs (top) exemplified for a nickel wire electrode. A, A*, and B are the first anodic, first cathodic, and the second anodic sweeps, respectively. c) Oxidation peaks of the nickel catalysts obtained after background subtraction of A−B, as demonstrated in b). All corresponding CVs can be found in **Figure S17.**

It is apparent from the still abundant presence of nanoparticles in cycled catalysts that they undergo a surface modification or bulk restructuring, reflected by the decreased metallic character. In parallel, consecutive CO stripping voltammetry experiments over the same sample yield progressively lower signals. Thus, it is reasonable to assume that CO produced over single atoms induces the evolution, leading to a passivating effect on neighboring nanoparticles. Control experiments in an argon saturated electrolyte (**Figure S22**) support this hypothesis evidencing a much less pronounced variation in the selectivity. Nevertheless, the presence of CO

cannot be the only factor provoking catalyst evolution, since no change in Faradaic efficiency is observed during 90 min of electrolysis at constant operating potential (**Figure S12**). This suggests that the variation of potential when being relaxed to OCP (typical values ranged from + 0.5 to +0.6 V vs. RHE) also has an influence. Indeed, when forcing the nanoparticle containing sample Ni_{CNP}/NC_{1223} to a potential step function while measuring reaction products at −0.6 V vs. RHE (**Figure 7, Figure S23**), catalyst evolution is observed as soon as potentials more positive than 0 V vs. RHE are temporarily applied. Based on these observations, we conclude that both the presence of CO and potential variations likely trigger a restructuring of nickel particles that renders them inactive toward hydrogen evolution. Due to the insufficient development of operando characterization techniques applicable to electrochemical conditions, the physical process of this surface restructuring might only be tentatively put forward. The visible presence of abundant nanoparticles in the cycled catalyst indicates that this is not caused by the dissolution of nickel into soluble Ni^{2+} ions, which is also thermodynamically unfavorable under the operating conditions applied.[50] A more reasonable explanation is that the nickel may transform into an oxidic state that is kinetically prevented from reduction back to the metallic form at the operating potential of -0.6 V vs RHE, therefore remaining inactive towards HER. Alternatively, the particles could be passivated by a thin carbon layer formed during the cycling although this could not be confirmed in STEM images of fresh and cycled samples.
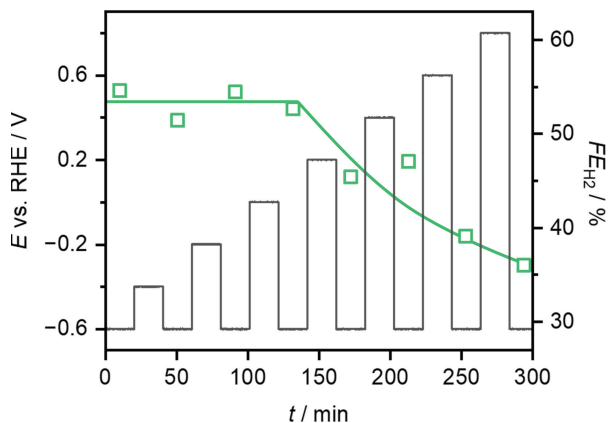
Figure 7. Evolution of the Faradaic efficiency towards HER (green symbols) for Ni_{CNP}/NC_{1223} while applying a potential step function (grey) temporarily forcing the system to increasingly oxidizing conditions. Quantification was performed after each step at the working potential of −0.6 V vs. RHE.

4. CONCLUSIONS

In summary, the results presented in this work demonstrated that high-performing nickel-based catalysts for eCO$_2$RR can be obtained over catalysts containing mixed metal entities. While single atoms showed high selectivity towards CO (FE_N = 82% at −0.6 V vs. RHE), not all nanoparticles displayed the same catalytic behavior. This was clearly evidenced by the vastly different performance observed for nanoparticles obtained from colloidal (FE_N < 45%) and impregnation approaches (FE_N = 78%). Remarkably, the systems containing colloidal particles reduced their activity toward the HER upon repeated exposure to reaction conditions, increasing their selectivity toward CO from 38 to 62%. The removal of particles by acid leaching led to a simultaneous decrease in the population of single atoms and the associated activity, demonstrating that these procedures might prohibit high activity. To rationalize the performance obtained over distinct nickel particles before and after cycling we applied CO stripping

25

voltammetry, highlighting its potential to assess their metallic character associated to undesired hydrogen evolution, which virtually disappeared after consecutive catalytic tests. Our study makes a significant contribution toward disentangling the influence of distinct nickel entities in eCO$_2$RR and further highlights the importance of considering dynamic effects in electrocatalytic systems.

ASSOCIATED CONTENT

Supporting physical (XPS, Raman, XRD, AES, and ADF-STEM) and electrochemical (Catalytic performance, CV) characterization of nickel catalysts and/or reference samples, schematic of the experimental setup.

AUTHOR INFORMATION

Corresponding Author

*Email: jpr@chem.ethz.ch

Present Addresses

Sean M. Collins, School of Chemical and Process Engineering and School of Chemistry, University of Leeds, Leeds LS2 9JT, United Kingdom.

Author Contributions

S.B., A.J.M, S.M., and J.P.R. designed, synthesized, physically characterized the materials, and performed electrochemical measurements and product analysis. F.K. and S.M.C. conducted microscopy. S.X. and A.B. conducted the XAS analysis. S.B., A.J.M., S.M., and J.P.R. wrote and edited the manuscript with input from all authors. All authors read and approved the final version of the manuscript.

Notes

The authors declare no competing financial interest.

REFERENCES

(1) Larrazábal, G. O.; Martín, A. J.; Pérez-Ramírez, J. Building Blocks for High Performance in Electrocatalytic CO_2 Reduction: Materials, Optimization Strategies, and Device Engineering. *J. Phys. Chem. Lett.* **2017**, 8, 3933-3944.

(2) Martín, A. J.; Pérez-Ramírez, J. Heading to Distributed Electrocatalytic Conversion of Small Abundant Molecules into Fuels, Chemicals, and Fertilizers. *Joule* **2019**, 3, 2602-2621.

(3) Yoshio, H.; Katsuhei, K.; Shin, S. Production of CO and CH_4 in Electrochemical Reduction of CO_2 at Metal Electrodes in Aqueos Hydrogencarbonate Solution. *Chem. Lett.* **1985**, 14, 1695-1698.

(4) Peterson, A. A.; Nørskov, J. K. Activity Descriptors for CO_2 Electroreduction to Methane on Transition-Metal Catalysts. *J. Phys. Chem. Lett.* **2012**, 3, 251-258.

(5) Peterson, A. A.; Abild-Pedersen, F.; Studt, F.; Rossmeisl, J.; Nørskov, J. K. How Copper Catalyzes the Electroreduction of Carbon Dioxide into Hydrocarbon Fuels. *Energy Environ. Sci.* **2010**, 3, 1311-1315.

(6) Hansen, H. A.; Varley, J. B.; Peterson, A. A.; Nørskov, J. K. Understanding Trends in the Electrocatalytic Activity of Metals and Enzymes for CO_2 Reduction to CO. *J. Phys. Chem. Lett.* **2013**, 4, 388-392.

(7) Bandarenka, A. S.; Koper, M. T. M. Structural and Electronic Effects in Heterogeneous Electrocatalysis: Toward a Rational Design of Electrocatalysts. *J. Catal.* **2013**, 308, 11-24.

(8) Calle-Vallejo, F.; Koper, M. T. M.; Bandarenka, A. S. Tailoring the catalytic activity of electrodes with monolayer amounts of foreign metals. *Chem. Soc. Rev.* **2013**, 42, 5210-5230.

(9)   Fang, Y.; Flake, J. C. Electrochemical Reduction of CO_2 at Functionalized Au Electrodes. *J. Am. Chem. Soc.* **2017**, 139, 3399-3405.

(10) García-Muelas, R.; Dattila, F.; Shinagawa, T.; Martín, A. J.; Pérez-Ramírez, J.; López, N. Origin of the Selective Electroreduction of Carbon Dioxide to Formate by Chalcogen Modified Copper. *J. Phys. Chem. Lett.* **2018**, 9, 7153-7159.

(11) Kwon, K. C.; Suh, J. M.; Varma, R. S.; Shokouhimehr, M.; Jang, H. W. Electrocatalytic Water Splitting and CO_2 Reduction: Sustainable Solutions via Single-Atom Catalysts Supported on 2D Materials. *Small Methods* **2019**, 3, 1800492.

(12) Su, X.; Yang, X. F.; Huang, Y.; Liu, B.; Zhang, T. Single-Atom Catalysis toward Efficient CO_2 Conversion to CO and Formate Products. *Acc. Chem. Res.* **2019**, 52, 656-664.

(13) Zhu, C.; Fu, S.; Shi, Q.; Du, D.; Lin, Y. Single-Atom Electrocatalysts. *Angew. Chem. Int. Ed.* **2017**, 56, 13944-13960.

(14) Ju, W.; Bagger, A.; Hao, G.-P.; Varela, A. S.; Sinev, I.; Bon, V.; Cuenya, B. R.; Kaskel, S.; Rossmeisl, J.; Strasser, P. Understanding Activity and Selectivity of Metal-Nitrogen-Doped Carbon Catalysts for Electrochemical Reduction of CO_2. *Nat. Commun.* **2017**, 8, 944.

(15) Long, C.; Li, X.; Guo, J.; Shi, Y.; Liu, S.; Tang, Z. Electrochemical Reduction of CO_2 over Heterogeneous Catalysts in Aqueous Solution: Recent Progress and Perspectives. *Small Methods* **2019**, 3, 1800369.

(16) Yan, C.; Lin, L.; Wang, G.; Bao, X. Transition Metal-Nitrogen Sites for Electrochemical Carbon Dioxide Reduction Reaction. *Chin. J. Catal.* **2019**, 40, 23-37.

(17) Ma, S.; Su, P.; Huang, W.; Jiang, S. P.; Bai, S.; Liu, J. Atomic Ni Species Anchored N-Doped Carbon Hollow Spheres as Nanoreactors for Efficient Electrochemical CO_2 Reduction. *ChemCatChem* **2019**, 11, 6092-6098.

(18) Jia, M.; Fan, Q.; Liu, S.; Qiu, J.; Sun, Z. Single-Atom Catalysis for Electrochemical CO_2 Reduction. *Current Opinion in Green and Sustainable Chemistry* **2019**, 16, 1-6.

(19) Büchele, S.; Chen, Z.; Mitchell, S.; Hauert, R.; Krumeich, F.; Pérez-Ramírez, J. Tailoring Nitrogen-Doped Carbons as Hosts for Single-Atom Catalysts. *ChemCatChem* **2019**, 11, 2812-2820.

(20) Pan, Y.; Zhang, C.; Liu, Z.; Chen, C.; Li, Y. Structural Regulation with Atomic-Level Precision: From Single-Atomic Site to Diatomic and Atomic Interface Catalysis. *Matter* **2020**, 2, 78-110.

(21) Jiang, R.; Li, L.; Sheng, T.; Hu, G.; Chen, Y.; Wang, L. Edge-Site Engineering of Atomically Dispersed Fe–N_4 by Selective C–N Bond Cleavage for Enhanced Oxygen Reduction Reaction Activities. *J. Am. Chem. Soc.* **2018**, 140, 11594-11598.

(22) Chen, Z.; Vorobyeva, E.; Mitchell, S.; Fako, E.; López, N.; Collins, S. M.; Leary, R. K.; Midgley, P. A.; Hauert, R.; Pérez-Ramírez, J. Single-Atom Heterogeneous Catalysts Based on Distinct Carbon Nitride Scaffolds. *Natl. Sci. Rev.* **2018**, 5, 642-652.

(23) Su, P.; Iwase, K.; Nakanishi, S.; Hashimoto, K.; Kamiya, K. Nickel-Nitrogen-Modified Graphene: An Efficient Electrocatalyst for the Reduction of Carbon Dioxide to Carbon Monoxide. *Small* **2016**, 12, 6083-6089.

(24) Liu, S.; Yang, H. B.; Hung, S.-F.; Ding, J.; Cai, W.; Liu, L.; Li, X.; Ren, X.; Kuang, Z.; Huang, Y.; Zhang, T.; Liu, B. Electrifying Model Single-Atom Catalyst for Elucidating the CO_2 Reduction Reaction. *Angew. Chem. Int. Ed.* **2019**, 59, 798-803.

(25) Yang, H. B.; Hung, S.-F.; Liu, S.; Yuan, K.; Miao, S.; Zhang, L.; Huang, X.; Wang, H.-Y.; Cai, W.; Chen, R.; Gao, J.; Yang, X.; Chen, W.; Huang, Y.; Chen, H. M.; Li, C. M.; Zhang,

T.; Liu, B. Atomically Dispersed Ni(I) as the Active Site for Electrochemical CO_2 Reduction. *Nat. Energy* **2018**, 3, 140-147.

(26) Li, J.; Pršlja, P.; Shinagawa, T.; Martín, A. J.; Krumeich, F.; Artyushkova, K.; Atanassov, P.; Zitolo, A.; Zhou, Y.; García-Muelas, R.; López, N.; Pérez-Ramírez, J.; Jaouen, F. Volcano Trend in Electrocatalytic CO_2 Reduction Activity over Atomically Dispersed Metal Sites on Nitrogen-Doped Carbon. *ACS Catal.* **2019**, 9, 10426-10439.

(27) Yan, C.; Li, H.; Ye, Y.; Wu, H.; Cai, F.; Si, R.; Xiao, J.; Miao, S.; Xie, S.; Yang, F.; Li, Y.; Wang, G.; Bao, X. Coordinatively Unsaturated Nickel–Nitrogen Sites Towards Selective and High-Rate CO_2 Electroreduction. *Energy Environ. Sci.* **2018**, 11, 1204-1210.

(28) Li, X.; Bi, W.; Chen, M.; Sun, Y.; Ju, H.; Yan, W.; Zhu, J.; Wu, X.; Chu, W.; Wu, C.; Xie, Y. Exclusive Ni-N_4 Sites Realize Near-Unity CO Selectivity for Electrochemical CO_2 Reduction. *J. Am. Chem. Soc.* **2017**, 139, 14889-14892.

(29) Jeong, H.-Y.; Balamurugan, M.; Choutipalli, V. S. K.; Jeong, E.-s.; Subramanian, V.; Sim, U.; Nam, K. T. Achieving Highly Efficient CO_2 to CO Electroreduction Exceeding 300 mA cm^{-2} with Single-Atom Nickel Electrocatalysts. *J. Mater. Chem. A* **2019**, 7, 10651-10661.

(30) De Luna, P.; Hahn, C.; Higgins, D.; Jaffer, S. A.; Jaramillo, T. F.; Sargent, E. H. What would it take for renewably powered electrosynthesis to displace petrochemical processes? *Science* **2019**, 364, eaav3506.

(31) Zheng, T.; Jiang, K.; Ta, N.; Hu, Y.; Zeng, J.; Liu, J.; Wang, H. Large-Scale and Highly Selective CO_2 Electrocatalytic Reduction on Nickel Single-Atom Catalyst. *Joule* **2019**, 3, 265-278.

(32) Gong, M.; Wang, D.-Y.; Chen, C.-C.; Hwang, B.-J.; Dai, H. J. A Mini Review on Nickel-Based Electrocatalysts For Alkaline Hydrogen Evolution Reaction. *Nano Res.* **2016**, 9, 28-46.

(33) Cheng, Y.; Zhao, S.; Johannessen, B.; Veder, J.-P.; Saunders, M.; Rowles, M. R.; Cheng, M.; Liu, C.; Chisholm, M. F.; De Marco, R.; Cheng, H.-M.; Yang, S.-Z.; Jiang, S. P. Atomically Dispersed Transition Metals on Carbon Nanotubes with Ultrahigh Loading for Selective Electrochemical Carbon Dioxide Reduction. *Adv. Mater.* **2018**, 30, 1706287-1706287.

(34) Zhao, C.; Wang, Y.; Li, Z.; Chen, W.; Xu, Q.; He, D.; Xi, D.; Zhang, Q.; Yuan, T.; Qu, Y.; Yang, J.; Zhou, F.; Yang, Z.; Wang, X.; Wang, J.; Luo, J.; Li, Y.; Duan, H.; Wu, Y.; Li, Y. Solid-Diffusion Synthesis of Single-Atom Catalysts Directly from Bulk Metal for Efficient CO_2 Reduction. *Joule* **2019**, 3, 584-594.

(35) Zhao, C.; Dai, X.; Yao, T.; Chen, W.; Wang, X.; Wang, J.; Yang, J.; Wei, S.; Wu, Y.; Li, Y. Ionic Exchange of Metal-Organic Frameworks to Access Single Nickel Sites for Efficient Electroreduction of CO_2. *J. Am. Chem. Soc.* **2017**, 139, 8078-8081.

(36) Jia, M.; Choi, C.; Wu, T.-S.; Ma, C.; Kang, P.; Tao, H.; Fan, Q.; Hong, S.; Liu, S.; Soo, Y.-L.; Jung, Y.; Qiu, J.; Sun, Z. Carbon-Supported Ni Nanoparticles for Efficient CO_2 Electroreduction. *Chem. Sci.* **2018**, 9, 8775-8780.

(37) Tan, D.; Cui, C.; Shi, J.; Luo, Z.; Zhang, B.; Tan, X.; Han, B.; Zheng, L.; Zhang, J.; Zhang, J. Nitrogen-Carbon Layer Coated Nickel Nanoparticles for Efficient Electrocatalytic Reduction of Carbon Dioxide. *Nano Res.* **2019**, 12, 1167-1172.

(38) Kalz, K. F.; Kraehnert, R.; Dvoyashkin, M.; Dittmeyer, R.; Gläser, R.; Krewer, U.; Reuter, K.; Grunwaldt, J.-D. Future Challenges in Heterogeneous Catalysis: Understanding Catalysts under Dynamic Reaction Conditions. *ChemCatChem* **2017**, 9, 17-29.

(39) Grosse, P.; Gao, D.; Scholten, F.; Sinev, I.; Mistry, H.; Roldan Cuenya, B. Dynamic Changes in the Structure, Chemical State and Catalytic Selectivity of Cu Nanocubes during CO_2 Electroreduction: Size and Support Effects. *Angew. Chem. Int. Ed.* **2018**, 57, 6192-6197.

(40) Larrazábal, G. O.; Martín, A. J.; Mitchell, S.; Hauert, R.; Pérez-Ramírez, J. Enhanced Reduction of CO_2 to CO over Cu–In Electrocatalysts: Catalyst Evolution Is the Key. *ACS Catal.* **2016**, 6, 6265-6274.

(41) Metin, Ö.; Mazumder, V.; Özkar, S.; Sun, S. Monodisperse Nickel Nanoparticles and their Catalysis in Hydrolytic Dehydrogenation of Ammonia Borane. *J. Am. Chem. Soc.* **2010**, 132, 1468-1469.

(42) Du, Y.; Zhu, Y.; Xi, S.; Yang, P.; Moser, H. O.; Breese, M. B. H.; Borgna, A. XAFCA: a new XAFS Beamline for Catalysis Research. *J. Synchrotorn Radiat.* **2015**, 22, 839-843.

(43) Ravel, B.; Newville, M. Athenal, Artemis, Hephaestus: Data Analysis for X-ray Absorption Spectroscopy Using IFEFFIT. *J. Synchrotron Radiat.* **2005**, 12, 537-541.

(44) Voiry, D.; Chhowalla, M.; Gogotsi, Y.; Kotov, N. A.; Li, Y.; Penner, R. M.; Schaak, R. E.; Weiss, P. S. Best Practices for Reporting Electrocatalytic Performance of Nanomaterials. *ACS Nano* **2018**, 12, 9635-9638.

(45) Borchardt, L.; Zhu, Q.-L.; Casco, M. E.; Berger, R.; Zhuang, X.; Kaskel, S.; Feng, X.; Xu, Q. Toward a Molecular Design of Porous Carbon Materials. *Mater. Today* **2017**, 20, 592-610.

(46) Arrigo, R.; Hävecker, M.; Schlögl, R.; Su, D. S. Dynamic Surface Rearrangement and Thermal Stability of Nitrogen Functional Groups on Carbon Nanotubes. *Chem. Commun.* **2008**, 4891-4893.

(47) Chastain, J., *Handbook of X-ray Photoelectron Spectroscopy*. Perkin-Elmer Corporation: 1992; Vol. 40, p 221.

(48) Graham, M.; Cohen, M. On The Mechanism of Low-Temperature Oxidation (23–450 C) of Polycrystalline Nickel. *J. Electrochem. Soc.* **1972**, 119, 879-882.

(49) Biesinger, M. C.; Lau, L. W. M.; Gerson, A. R.; Smart, R. S. C. The Role of the Auger Parameter in XPS Studies of Nickel Metal, Halides and Oxides. *Phys. Chem. Chem. Phys.* **2012**, 14, 2434-2442.

(50) Huang, L.-F.; Hutchison, M. J.; Santucci, R. J.; Scully, J. R.; Rondinelli, J. M. Improved Electrochemical Phase Diagrams from Theory and Experiment: The Ni–Water System and its Complex Compounds. *J. Phys. Chem. C.* **2017**, 121, 9782-9789.

(51) Cheng, Y.; Zhao, S. Y.; Li, H. B.; He, S.; Veder, J.-P.; Johannessen, B.; Xiao, J.; Lu, S.; Pan, J.; Chisholm, M. F.; Yang, S.-Z.; Liu, C.; Chen, J. G.; Jiang, S. P. Unsaturated Edge-Anchored Ni Single Atoms on Porous Microwave Exfoliated Graphene Oxide for Electrochemical CO_2. *Appl. Catal. B* **2019**, 243, 294-303.

(52) Ford, R. R. In *Advances in Catalysis*, Eley, D. D., Pines, H., Weisz, P. B., Eds. Academic Press: 1970; Vol. 21, p 51-150.

(53) Gisbert, R.; García, G.; Koper, M. T. M. Oxidation of Carbon Monoxide on Poly-Oriented and Single-Crystalline Platinum Electrodes over a Wide Range of pH. *Electrochim. Acta* **2011**, 56, 2443-2449.

(54) Hall, D. S.; Bock, C.; MacDougall, B. R. The Electrochemistry of Metallic Nickel: Oxides, Hydroxides, Hydrides and Alkaline Hydrogen Evolution. *J. Electrochem. Soc.* **2013**, 160, F235-F243.

TABLE OF CONTENTS GRAPHIC